SOLAR CELLS

Carrier lifetimes of >1 µs in Sn-Pb perovskites enable efficient all-perovskite tandem solar cells

Jinhui Tong[1,2]*, **Zhaoning Song**[3]*, **Dong Hoe Kim**[1]†, **Xihan Chen**[1], **Cong Chen**[3], **Axel F. Palmstrom**[1], **Paul F. Ndione**[1], **Matthew O. Reese**[1], **Sean P. Dunfield**[1,2,4], **Obadiah G. Reid**[1,2], **Jun Liu**[1], **Fei Zhang**[1], **Steven P. Harvey**[1], **Zhen Li**[1], **Steven T. Christensen**[1], **Glenn Teeter**[1], **Dewei Zhao**[3], **Mowafak M. Al-Jassim**[1], **Maikel F. A. M. van Hest**[1], **Matthew C. Beard**[1], **Sean E. Shaheen**[2,5], **Joseph J. Berry**[1]‡, **Yanfa Yan**[3]‡, **Kai Zhu**[1]‡

All-perovskite–based polycrystalline thin-film tandem solar cells have the potential to deliver efficiencies of >30%. However, the performance of all-perovskite–based tandem devices has been limited by the lack of high-efficiency, low–band gap tin-lead (Sn-Pb) mixed-perovskite solar cells (PSCs). We found that the addition of guanidinium thiocyanate (GuaSCN) resulted in marked improvements in the structural and optoelectronic properties of Sn-Pb mixed, low–band gap (~1.25 electron volt) perovskite films. The films have defect densities that are lower by a factor of 10, leading to carrier lifetimes of greater than 1 microsecond and diffusion lengths of 2.5 micrometers. These improved properties enable our demonstration of >20% efficient low–band gap PSCs. When combined with wider–band gap PSCs, we achieve 25% efficient four-terminal and 23.1% efficient two-terminal all-perovskite–based polycrystalline thin-film tandem solar cells.

S ingle-junction organic-inorganic metal-halide perovskite solar cells (PSCs) have seen rapid development and an increase of power conversion efficiencies (PCEs) from <4% to a certified 23.7% (*1–4*). The majority of research efforts have centered on Pb-based perovskites with band gaps of ~1.5 to 1.7 eV (*3, 5–12*). Replacing Pb, either partially or completely, with Sn would enable band gap reductions to ~1.2 eV while retaining reasonable solar cell performance (*13–19*), which would open a pathway for preparing all-perovskite–based polycrystalline thin-film tandem solar cells that could achieve high efficiency (>30%) while retaining low manufacturing cost and flexible form factors (*20–24*).

At present, the all-perovskite tandem cell PCE is 20 to 23% for four-terminal (4-T) and 17 to 21% for two-terminal (2-T) configurations (*13, 15, 23, 25–27*). Reaching a >30% efficient all-perovskite thin-film tandem solar cell requires the low–band gap absorber to be at least 21 to 22% efficient. Thus, high-quality Sn-Pb low–band gap perovskite thin films with greater than micrometer thickness are needed to permit

sufficient light harvesting, as well as several micrometer-long carrier diffusion lengths to ensure effective charge-carrier transport and extraction (*21, 24*). State-of-the-art low–band gap (1.2 to 1.3 eV) PSCs based on Sn-Pb mixed perovskites have reported PCEs of ~18% (*14–16, 18*) that are lower than those of their pure-Pb counterparts (band gaps between 1.5 and 1.6 eV) with PCEs between 21 and 23% (*3, 4, 6, 7*), even though Sn-Pb–based perovskites have a band gap that allows a larger fraction of the solar spectrum to be absorbed.

The lower performance of Sn-Pb mixed low–band gap PSCs arises from both materials and device issues. The high defect density associated with Sn^{2+} oxidation limits carrier lifetime and charge collection, and additives such as SnF_2 (*28, 29*), SnF_2-pyrazine complex (*30*), or fluoroalkyl-substituted fullerene (*31*) have been used to suppress the defect density. It has also proven difficult to synthesize uniform, pinhole-free, Sn-based thin films because Sn-based perovskite films crystallize rapidly (*32*). Despite the several strategies (e.g., lattice strain, interface energetics, halide alloying) explored to improve the performance of low–band gap Sn-Pb–based PSCs (*14, 16, 18*), their performance in tandem PSCs has lagged behind that of their Pb counterparts.

We report using guanidinium thiocyanate (GuaSCN) to improve the structural and opto-electronic properties of low–band gap (1.25 eV) perovskite thin films [$(FASnI_3)_{0.6}(MAPbI_3)_{0.4}$, where FA and MA denote formamidinium and methylammonium, respectively] in several ways. This method (i) reduced energetic disorder, with defect densities decreased by a factor of >10; (ii) increased carrier lifetimes to >1 µs; (iii) increased carrier diffusion length from ~500 nm to 2.5 µm; (iv) reduced surface recombination

velocity by about a factor of 10, to 1.0×10^2 cm/s; and (v) improved film morphology, resulting in fewer structural defects. We attribute these improvements to the formation of two-dimensional (2D) structures at grain boundaries that appeared to passivate grain boundaries, suppress the formation of excessive Sn vacancies, and enhance the stability of low–band gap perovskite films. With these improved properties, we have demonstrated >20% efficient, 1.25-eV, low–band gap, single-junction PSCs. When combined with wider–band gap PSCs, we achieve 25% efficient 4-T and 23.1% efficient 2-T all-perovskite–based polycrystalline thin-film tandem cells.

We used $(FASnI_3)_{0.6}(MAPbI_3)_{0.4}$ as the baseline composition for the low–band gap perovskite (*15*). The films were prepared by spin-coating a stoichiometric mixture of components (FAI, SnI_2, MAI, and PbI_2) and SnF_2 in a mixed solvent of dimethyl formamide and dimethyl sulfoxide (DMF/DMSO). These perovskite films were modified by adding GuaSCN at various molar ratios with respect to MAI. The device stack used was glass/indium tin oxide (ITO)/poly(3,4-ethylenedioxythiophene)-poly(styrenesulfonate) (PEDOT:PSS)/perovskite/fullerene (C_{60})/bathocuproine (BCP)/silver (Ag). Figure 1A compares the typical photocurrent density–voltage (*J-V*) curves of PSCs based on the low–band gap $(FASnI_3)_{0.6}(MAPbI_3)_{0.4}$ perovskite thin films prepared with and without addition of 7% GuaSCN; the detailed photovoltaic (PV) parameters are given in table S1. The cross-sectional scanning electron microscope (SEM) image of a typical PSC is shown in fig. S1. Devices with or without GuaSCN exhibited negligible hysteresis (<0.5%) between forward- and reverse-scan *J-V* curves. For 7% GuaSCN, the device PCE improved from 15.3% to 18.4% because of increases in short-circuit photocurrent density (J_{sc}) by ~1 mA/cm², open-circuit voltage (V_{oc}) by ~60 mV, and fill factor (FF) by ~6%. The statistical comparison of device parameters is shown in Fig. 1B (for 20 devices each). The external quantum efficiency (EQE) spectra of the two devices are shown in Fig. 1C; the integrated photocurrent density over the AM 1.5G solar spectrum is within 3% of the values obtained from *J-V* characterization.

We examined the impact of varying GuaSCN concentration (0 to 50%) on the device characteristics. All PV parameters showed a systematic improvement when the proportion of GuaSCN was increased from 0% to 7%, followed by a decrease in the parameters with a further increase of GuaSCN from 10% to 50% (fig. S2). The improvement of the device performance associated with the addition of GuaSCN was attributed to a combination of effects resulting from the GuaSCN, rather than the individual effect of Gua^+ and SCN^- when used separately. Figure S3 compares the device characteristics of PSCs based on low–band gap perovskite films prepared without and with different additives [GuaI, $Pb(SCN)_2$, and GuaSCN]. Although both GuaI and $Pb(SCN)_2$ increased device performance, the respective improvements were lower than that seen in the devices prepared with the GuaSCN additive.
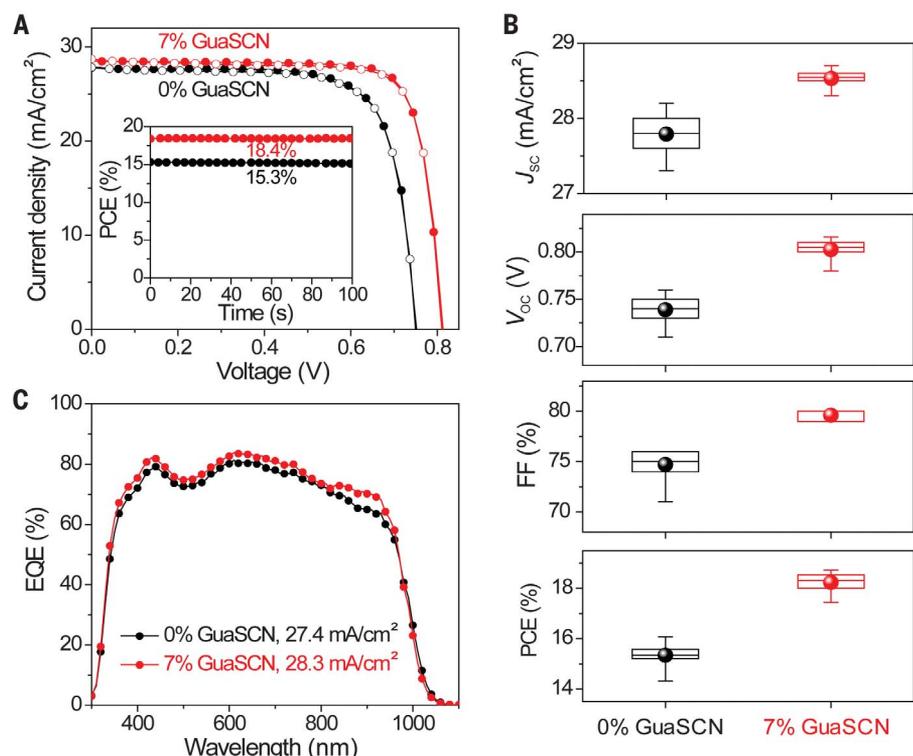
Fig. 1. Comparison of device characteristics. (**A** and **B**) Typical photocurrent density–voltage (*J-V*) curves (with inset showing the stable power outputs) (A) and statistical comparison (B) of *J-V* parameters of low–band gap PSCs prepared with or without 7% GuaSCN additive. The mean value, maximum and minimum values, and 25% to 75% region of data are represented by the circle, top/bottom bars, and rectangle, respectively. (**C**) External quantum efficiency of the two devices shown in (A) with the integrated current density indicated.
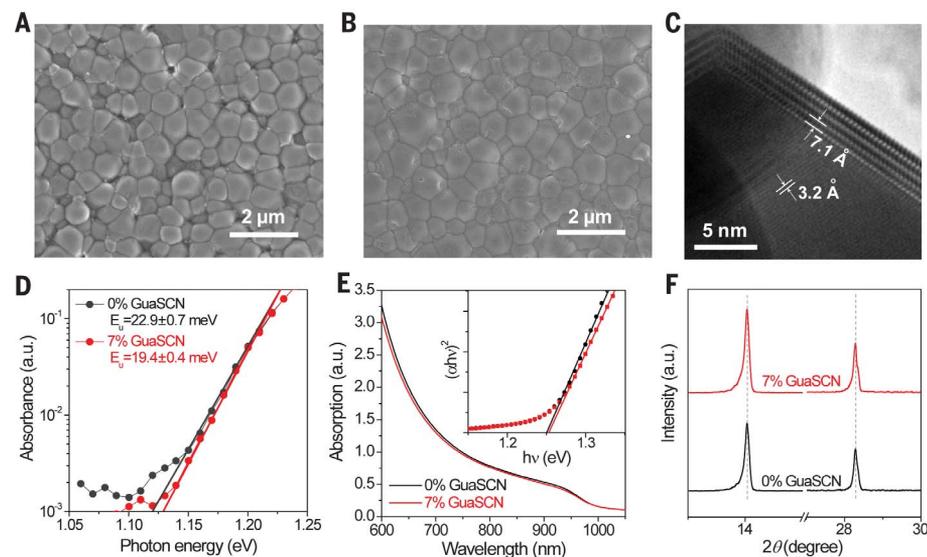

Fig. 2. Optical and structural characterizations. (**A** and **B**) SEM images of perovskite films prepared without (A) and with (B) 7% GuaSCN additive. (**C**) HRTEM image of the grain boundary region of perovskite prepared with 7% GuaSCN additive. (**D**) Comparison of photothermal deflection spectroscopy (PDS) measurements of energetic disorder. The Urbach energies determined by the best fits are 19.4 ± 0.4 meV and 22.9 ± 0.7 meV for the samples with and without the use of 7% GuaSCN, respectively. (**E** and **F**) Ultraviolet-visible absorption spectra (with inset showing the Tauc analyses) (E) and x-ray diffraction patterns (F) for low–band gap perovskite thin films prepared with and without 7% GuaSCN modifier.

We performed various structural and optoelectronic characterizations of GuaSCN-modified $(FASnI_3)_{0.6}(MAPbI_3)_{0.4}$ perovskite thin films. The improvement in film quality after adding an optimal amount of GuaSCN was the result of the known effect of SCN ions increasing grain size and improving film morphology (*15, 33, 34*). Without GuaSCN, the Sn-Pb mixed-perovskite thin films contained many small grains, pinholes, and gaps at grain boundaries (Fig. 2A), where defects can easily form that lead to high levels of nonradiative recombination. With 7% GuaSCN additive, the densities of small grains and pinholes were substantially reduced and grain boundaries became more compact (Fig 2B; see fig. S4 for morphology changes with 0% to 50% GuaSCN addition).

Optimal GuaSCN addition also reduced the defect states in grains and grain boundary/surface regions. The most abundant defects in Sn-Pb perovskite are Sn vacancies created by oxidation of Sn^{2+} to Sn^{4+}, which is desirable only at small concentrations for p-type doping. Additives such as SnF_2 can suppress the defect density in Sn- or Sn-Pb–based perovskites (*28, 29*). A high-resolution transmission electron microscopy (HRTEM) image (Fig. 2C) confirmed that a 2D structure formed at grain boundaries with a small amount of GuaSCN additive. Time-of-flight secondary ion mass spectroscopy (TOF-SIMS) tomography showed that Gua^+ and SCN^- ions tended to segregate to grain boundaries (fig. S5). The presence of Gua is consistent with an x-ray photoelectron spectroscopy (XPS) measurement (fig. S6), but the precise composition cannot be determined because of the myriad components (i.e., mixed MA/FA, Sn/Pb, and/or I/SCN) used in this formulation. The formation of such 2D structure could improve the perovskite electronic properties by (i) passivating grain boundaries and surfaces through its much wider band gap; (ii) blocking diffusion of Sn out of grains and further suppressing the formation of excessive Sn vacancies; and (iii) reducing oxygen diffusion into grains through surface and grain boundaries to suppress further oxidation of Sn^{2+}. The reduced defect density was confirmed by Sn 3d core-level XPS analysis (fig. S7).

We further studied the effects of reduced defect density of our Sn-Pb perovskite thin films using photothermal deflection spectroscopy (PDS). The addition of 7% GuaSCN in the precursor reduced the Urbach energy (E_u) from 22.9 to 19.4 meV (Fig. 2D), which suggests less energetic disorder associated with fewer sub–band gap states. A combination of dark and photoinduced microwave conductivity measurements showed that the dark carrier density was reduced by a factor of ~10, from 2.8×10^{17} cm^{-3} for the control (0% GuaSCN) sample to 1.7×10^{16} cm^{-3} for the 7% GuaSCN–modified sample (fig. S8), consistent with the suppressed oxidation of Sn^{2+} to Sn^{4+} states (*29, 35*).

The much-improved electronic properties enabled us to increase the thickness of low–band gap Sn-Pb perovskite absorber film up to 1 μm without sacrificing V_{oc} and FF. Shown in Fig. 2, E and F, respectively, are the ultraviolet-visible absorption spectra and x-ray diffraction (XRD) patterns of the perovskite thin films. The

addition of 7% GuaSCN did not affect the band gap of ~1.25 eV and there was no shift in the XRD diffraction peaks. Thus, at low concentrations, the GuaSCN additive may not have been incorporated into perovskite lattice. Two-

dimensional XRD measurements suggested that the 7% GuaSCN additive did not affect the orientation of perovskite grains (fig. S9). However, the absorption onset was blue-shifted (fig. S10), reflecting increased band gaps for 20% GuaSCN

(~1.28 eV) and for 50% GuaSCN (~1.31 eV). For GuaSCN concentrations of 20% or more, some Gua and SCN was forced into the lattice of Sn-Pb perovskites, and increased in the lattice constant (fig. S11). High concentrations of GuaSCN also

Fig. 3. Charge-carrier dynamics. (**A** and **B**) Time-resolved photoluminescence measurement of the carrier lifetime of low–band gap perovskite thin films prepared without (A) and with (B) the use of 7% GuaSCN modifier. The average carrier lifetimes, ⟨τ⟩, determined from bi-exponential fittings (blue solid lines) are 139 ns and 1232 ns for the samples without and with the use of 7% GuaSCN, respectively. (**C** and **D**) Comparison of transient reflectance spectroscopy measurement of carrier diffusion and surface recombination of low–band gap perovskite thin films prepared without (C) and with (D) the use of 7% GuaSCN modifier. The blue solid lines are nonlinear least-squares global best-fit curves for the two samples. The carrier diffusion coefficient, D, and surface recombination velocity (SRV; denoted as S) determined from the global fittings are $D = 0.02$ cm^2/s and $S = 1.3 \times 10^3$ cm/s for the control (0% GuaSCN) sample, and $D = 0.05$ cm^2/s and $S = 1.0 \times 10^2$ cm/s for the sample using 7% GuaSCN modifier.
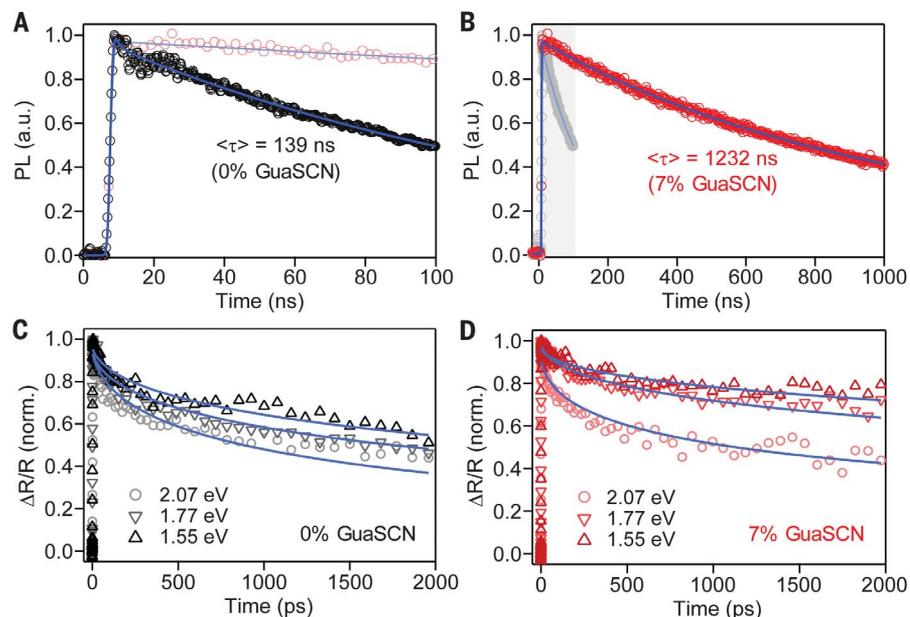

Fig. 4. Champion low–band gap perovskite single-junction and perovskite-perovskite tandem solar cells. (**A**) Cross-sectional SEM image of the low–band gap PSC using the GuaSCN-modified (FASnI$_3$)$_{0.6}$(MAPbI$_3$)$_{0.4}$ perovskite film. (**B**) J-V curve of the champion low–band gap PSC; the inset shows the SPO efficiency near the maximum power point (MPP). (**C**) EQE spectrum of the device shown in (B); the integrated photocurrent density is indicated. (**D**) J-V curves of a semitransparent wide–band gap PSC using a transparent IZO top contact and the filtered low–band gap PSC using the top semitransparent PSC as the optical filter. (**E**) EQE spectra of the semitransparent top wide–band gap PSC and the filtered bottom low–band gap PSC. The integrated photocurrent densities are indicated. (**F** and **G**) SPO efficiencies (F) and MPP tracking (G) of the semitransparent wide–band gap top PSC, the filtered bottom low–band gap PSC, and the 4-T tandem device under simulated AM 1.5G one-sun illumination. (**H**) MPP tracking comparison of the filtered control and GuaSCN-modified low–band gap PSCs. (**I** and **J**) Device characteristics of 2-T all-perovskite tandem solar cells. (**I**) J-V curves of the 2-T tandem cell. Inset shows the EQE spectra of the top and bottom subcells, respectively. (**J**) SPO efficiency and MPP tracking (inset) of the 2-T tandem cell under one-sun illumination.
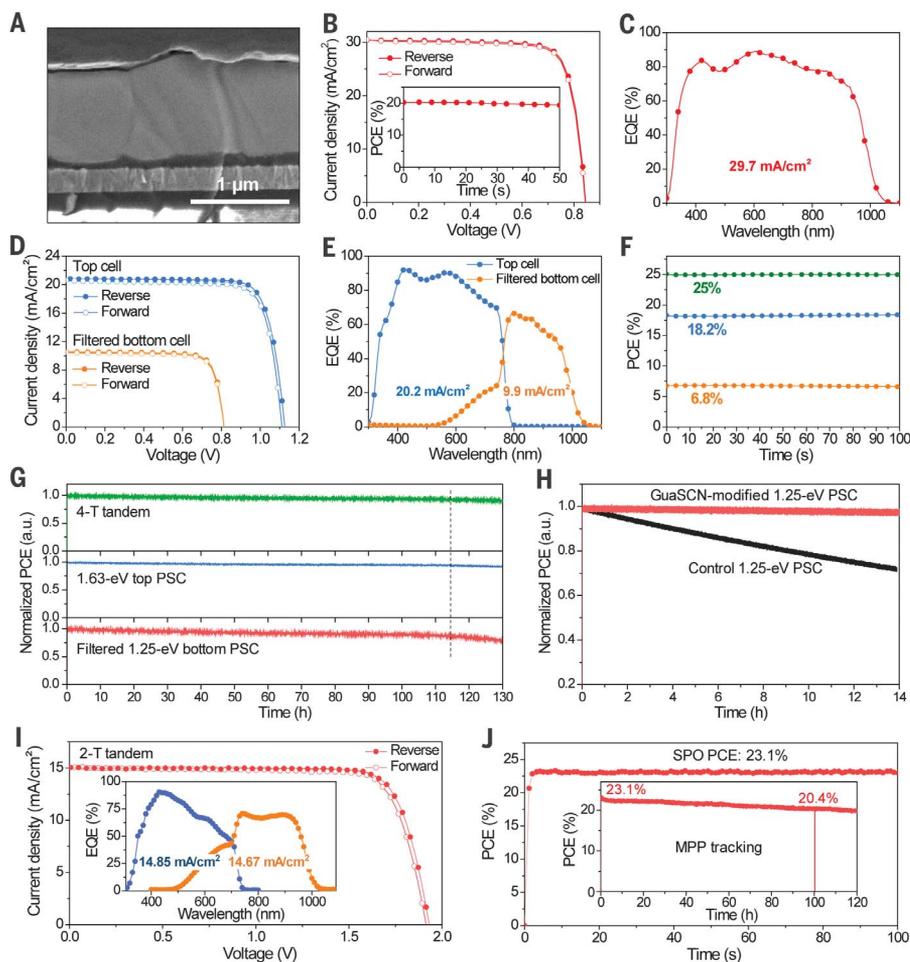
created more structural defects (e.g., pinholes) mainly formed during grain growth (fig. S12), likely caused by greater strain created by the much larger Gua ions relative to FA and MA.

Recent progress in the development of Sn- or Sn-Pb–based PSCs has improved carrier lifetimes from <1 ns to ~255 ns, leading to the demonstration of >17% efficient, low–band gap (1.25 eV) PSCs (15). Figure 3, A and B, compares the impact of adding 7% GuaSCN in the perovskite precursor on the average carrier lifetime τ (or $\langle\tau\rangle$) for the 1.25-eV perovskite thin films based on biexponential fittings of the time-resolved photoluminescence curves (see table S2 for fitting parameters). The lifetime of ~139 ns was increased to 1232 ns for 7% GuaSCN, which is comparable to state-of-the-art pure Pb–based perovskite thin films. This increase of carrier lifetime is consistent with the much-reduced dark carrier density and Urbach energy.

We further examined these films using transient reflection (TR) spectroscopy (36, 37), which measures the surface carrier dynamics, from which we can obtain both the carrier diffusion coefficient (D) and the surface recombination velocity (SRV, denoted as S) (36, 37). Changing the pump photon energies created a different surface carrier distribution profile, and by simultaneously modeling the decay of charge carriers within a global fitting procedure that includes both diffusion and surface recombination for the different charge carrier distributions, best-fit values of D and S values were obtained (37) (see supplementary materials). The decay dynamics observed within the 2-ns time window (Fig. 3, C and D) mainly arose from diffusion and surface recombination of surface charge carriers. Adding 7% GuaSCN improved D values from 0.02 cm^2/s to 0.05 cm^2/s and S values from 1.3×10^3 cm/s to 1.0×10^2 cm/s. The carrier diffusion lengths L_D, calculated from $\sqrt{D \times \tau}$, were 0.53 μm for the control and 2.5 μm for 7% added GuaSCN. Because the Sn-Pb mixed low–band gap perovskites have lower absorption cross sections than pure Pb–based perovskites, longer L_D can enable the use of a thicker Sn-Pb perovskite thin film to harvest more light (especially in the near-infrared region) and to collect the converted photocarriers without substantial recombination loss.

The factor of 10 reduction of SRV with the use of 7% GuaSCN (decreasing from ~1.3×10^3 cm/s

to 1.0×10^2 cm/s) is consistent with the much longer carrier lifetime and faster carrier transport observed above. It is noteworthy that the SRV of 1.0×10^2 cm/s for the GuaSCN-modified $(FASnI_3)_{0.6}(MAPbI_3)_{0.4}$ sample is comparable to the values (~10 to 100 cm/s) reported for other high-efficiency PV absorbers in which sophisticated passivation is used (38–40).

Figure 4A shows a cross-sectional SEM image of the device based on a 7% GuaSCN-modified $(FASnI_3)_{0.6}(MAPbI_3)_{0.4}$ perovskite absorber of ~1-μm thickness, and Fig. 4B shows the J-V curves for the champion PSC of this type. Negligible hysteresis was observed in the reverse and forward J-V scans. The PCEs determined from J-V curves reached 20.5% and 20.4% from the reverse and forward J-V scans, respectively. The corresponding stable power output (SPO) efficiency is ~20.2% (Fig. 4B, inset). The detailed PV parameters are given in Table 1, and the statistical distribution of PV parameters is given in fig. S13. There was no substantial drop in cell efficiency when the cell size was increased to 0.12 cm^2 (fig. S14). In comparison to the device based on a 580-nm-thick perovskite layer (Fig. 1A and table S1), the performance improvement from the 1-μm cell results primarily from the enhanced J_{sc}—from 28.5 to 30.4 mA/cm^2 in the reverse scan and from 28.7 to 30.5 mA/cm^2 in the forward scan—which matched well with the EQE spectrum (Fig. 4C) and was consistent with the enhanced optoelectronic properties. The FF and V_{oc} parameters actually improved slightly.

The improved electronic properties of low–band gap Sn-Pb perovskite films allowed us to fabricate efficient all-perovskite tandem solar cells. We first combined semitransparent PSCs based on 1.63-eV $Cs_{0.05}FA_{0.8}MA_{0.15}PbI_{2.55}Br_{0.45}$ perovskite absorbers with the 1.25-eV low–band gap PSC to construct all-perovskite, 4-T tandem solar cells. The J-V characteristics of the semitransparent 1.63-eV PSC with an indium-doped zinc oxide (IZO) top transparent contact (Fig. 4D) had a PCE of 18.5% from the reverse scan, 18.0% from the forward scan, and 18.2% from the SPO measurement (Table 1). The schematic of the semitransparent device stack is shown in fig. S15. The transmittance spectrum of the semitransparent cell is shown in fig. S16. Using the top semitransparent PSC as the optical filter, the filtered 1.25-eV bottom PSC had PCEs of 6.8% and 6.7%

from the reverse- and forward-scan J-V curves, respectively (Fig. 4D). The corresponding EQE spectra and SPO results for the top semitransparent 1.63-eV PSC and the filtered bottom 1.25-eV PSC are shown in Fig. 4, E and F, respectively. The 4-T all-perovskite tandem device had PCEs of 25.4% and 24.7% from the reverse- and forward-scan J-V curves, respectively, with an efficiency of 25.0% from the SPO measurement (Table 1).

We examined the operational stability of the semitransparent wide–band gap PSC, the filtered low–band gap PSC, and the corresponding 4-T tandem device by maximum power point (MPP) tracking under simulated AM 1.5G one-sun illumination (Fig. 4G). The 1.25-eV low–band gap PSC was encapsulated with cover glass and ultraviolet-curable epoxy. During the initial ~115 hours of MPP tracking, the devices showed approximately a linear degradation over time: ~0.09% per hour (T80 of ~222 hours; T80 is the time at which PCE degrades to 80% of the initial value) for the 1.25-eV PSC, ~0.04% per hour (T80 of ~500 hours) for the 1.63-eV PSC, and ~0.05% per hour (T80 of ~400 hours) for the 4-T tandem device. In contrast, the 1.25-eV control device (no GuaSCN) exhibited a T80 of only ~8.5 hours under the same operating conditions (Fig. 4H). The devices, especially the 1.25-eV PSC, exhibited more degradation after ~115 hours of MPP tracking, which is attributable to the corrosion of the Ag electrode.

We then fabricated 2-T all-perovskite tandem cells by combining a 1.75-eV wide–band gap PSC with a 1.25-eV low–band gap PSC. The 1.75-eV perovskite is a better match to the 1.25-eV perovskite with complementary absorption for constructing 2-T tandem cells. Fig. 4I shows the J-V curves, EQE, SPO efficiency, and MPP tracking of the champion 2-T all-perovskite tandem cell. We followed our previously published procedures for tandem cell integration (23). The active area of the 2-T tandem cell is 0.105 cm^2 as defined by the mask. Fig. 4I shows that when measured under the reverse voltage scan, the 2-T tandem cell achieved a PCE of 23.4% with a J_{sc} of 15.01 mA/cm^2, V_{oc} of 1.942 V, and FF of 80.31%. When measured under the forward voltage scan, the 2-T tandem cell showed a PCE of 22.9% with a J_{sc} of 14.99 mA/cm^2, V_{oc} of 1.915 V, and FF of 79.76%. The corresponding SPO efficiency is 23.1% (Fig. 4J). The EQE spectra (Fig. 4I, inset) from the top and bottom perovskite subcells, when

Table 1. PV parameters of low–band gap perovskite single-junction and perovskite-perovskite four-terminal tandem solar cells.

Device		J_{sc} (mA cm^{-2})	V_{oc} (V)	FF (%)	PCE (%)	SPO (%)
1.63-eV PSC (semitransparent)	Forward	20.6	1.113	78.5	18.0	18.2
	Reverse	20.8	1.124	79.3	18.5	
1.25-eV PSC	Forward	30.5	0.834	80.0	20.4	20.2
	Reverse	30.4	0.834	80.8	20.5	
Filtered 1.25-eV PSC	Forward	10.5	0.806	79.5	6.7	6.8
	Reverse	10.5	0.806	80.6	6.8	
4-terminal tandem	Forward	–	–	–	24.7	25.0
	Reverse	–	–	–	25.4	

integrated over the AM 1.5G solar spectrum, yield current densities of 14.85 and 14.67 mA/cm^2, respectively. We further checked the operational stability of the 2-T tandem cell by MPP tracking under simulated AM 1.5G one-sun illumination (Fig. 4J, inset). More than 88% of the initial efficiency was maintained after 100 hours of continuous operation.

REFERENCES AND NOTES

1. A. Kojima, K. Teshima, Y. Shirai, T. Miyasaka, *J. Am. Chem. Soc.* **131**, 6050–6051 (2009).
2. N.-G. Park, M. Grätzel, T. Miyasaka, K. Zhu, K. Emery, *Nat. Energy* **1**, 16152 (2016).
3. W. S. Yang et al., *Science* **356**, 1376–1379 (2017).
4. National Renewable Energy Laboratory, Best Research-Cell Efficiencies (2019); www.nrel.gov/pv/assets/pdfs/ pv-efficiency-chart.20190103.pdf.
5. M. M. Lee, J. Teuscher, T. Miyasaka, T. N. Murakami, H. J. Snaith, *Science* **338**, 643–647 (2012).
6. M. Saliba et al., *Science* **354**, 206–209 (2016).
7. X. Zheng et al., *Nat. Energy* **2**, 17102 (2017).
8. H. Tan et al., *Science* **355**, 722–726 (2017).
9. D. P. McMeekin et al., *Science* **351**, 151–155 (2016).
10. D. Shi et al., *Science* **347**, 519–522 (2015).
11. Y. Lin et al., *Adv. Mater.* **29**, 1700607 (2017).
12. J. Ávila, C. Momblona, P. P. Boix, M. Sessolo, H. J. Bolink, *Joule* **1**, 431–442 (2017).
13. G. E. Eperon et al., *Science* **354**, 861–865 (2016).
14. Z. Yang, A. Rajagopal, A. K.-Y. Jen, *Adv. Mater.* **29**, 1704418 (2017).
15. D. Zhao et al., *Nat. Energy* **2**, 17018 (2017).
16. G. Kapil et al., *Nano Lett.* **18**, 3600–3607 (2018).
17. F. Hao, C. C. Stoumpos, R. P. H. Chang, M. G. Kanatzidis, *J. Am. Chem. Soc.* **136**, 8094–8099 (2014).
18. R. Prasanna et al., *J. Am. Chem. Soc.* **139**, 11117–11124 (2017).
19. S. Shao et al., *Adv. Mater.* **30**, 1803703 (2018).
20. G. E. Eperon, M. T. Hörantner, H. J. Snaith, *Nat. Rev. Chem.* **1**, 0095 (2017).
21. T. Leijtens, K. A. Bush, R. Prasanna, M. D. McGehee, *Nat. Energy* **3**, 828–838 (2018).
22. J. J. Berry et al., *ACS Energy Lett.* **2**, 2540–2544 (2017).
23. D. Zhao et al., *Nat. Energy* **3**, 1093–1100 (2018).
24. M. T. Hörantner et al., *ACS Energy Lett.* **2**, 2506–2513 (2017).
25. A. Rajagopal et al., *Adv. Mater.* **29**, 1702140 (2017).
26. D. Forgács et al., *Adv. Energy Mater.* **7**, 1602121 (2017).
27. D. Zhao et al., *ACS Energy Lett.* **3**, 305–306 (2018).
28. L. Ma et al., *J. Am. Chem. Soc.* **138**, 14750–14755 (2016).
29. W. Liao et al., *Adv. Mater.* **28**, 9333–9340 (2016).
30. S. J. Lee et al., *J. Am. Chem. Soc.* **138**, 3974–3977 (2016).
31. A. Rajagopal, P.-W. Liang, C.-C. Chueh, Z. Yang, A. K. Y. Jen, *ACS Energy Lett.* **2**, 2531–2539 (2017).
32. T. Yokoyama et al., *J. Phys. Chem. Lett.* **7**, 776–782 (2016).
33. W. Ke et al., *Adv. Mater.* **28**, 5214–5221 (2016).
34. S. P. Harvey et al., *ACS Appl. Mater. Interfaces* **10**, 28541–28552 (2018).
35. M. H. Kumar et al., *Adv. Mater.* **26**, 7122–7127 (2014).
36. Y. Yang et al., *Nat. Commun.* **6**, 7961 (2015).
37. Y. Yang et al., *Nat. Energy* **2**, 16207 (2017).
38. W. J. Royea, A. Juang, N. S. Lewis, *Appl. Phys. Lett.* **77**, 1988–1990 (2000).
39. R. Cohen, V. Lyahovitskaya, E. Poles, A. Liu, Y. Rosenwaks, *Appl. Phys. Lett.* **73**, 1400–1402 (1998).
40. X.-H. Zhao et al., *Appl. Phys. Lett.* **105**, 252101 (2014).

Science

Carrier lifetimes of >1 μs in Sn-Pb perovskites enable efficient all-perovskite tandem solar cells

Jinhui Tong, Zhaoning Song, Dong Hoe Kim, Xihan Chen, Cong Chen, Axel F. Palmstrom, Paul F. Ndione, Matthew O. Reese, Sean P. Dunfield, Obadiah G. Reid, Jun Liu, Fei Zhang, Steven P. Harvey, Zhen Li, Steven T. Christensen, Glenn Teeter, Dewei Zhao, Mowafak M. Al-Jassim, Maikel F. A. M. van Hest, Matthew C. Beard, Sean E. Shaheen, Joseph J. Berry, Yanfa Yan and Kai Zhu

Efficient all-perovskite tandem cells

Organic-inorganic perovskite films can boost the output of conventional silicon solar cells in tandem geometries by utilizing more of the light at the blue end of the solar spectrum. Tandem cells that use only perovskite films have been less successful because of the lack of a suitable material with a low bandgap that can replace silicon. Tong *et al.* report that a mixed tin-lead organic-inorganic material containing a small fraction of guanidinium thiocyanate has a low bandgap, long charge-carrier lifetime, and efficiencies around 25%.
Science, this issue p. 475

ARTICLE TOOLS	http://science.sciencemag.org/content/364/6439/475
SUPPLEMENTARY MATERIALS	http://science.sciencemag.org/content/suppl/2019/04/17/science.aav7911.DC1
REFERENCES	This article cites 43 articles, 7 of which you can access for free http://science.sciencemag.org/content/364/6439/475#BIBL
PERMISSIONS	http://www.sciencemag.org/help/reprints-and-permissions

Use of this article is subject to the Terms of Service